RESEARCH ARTICLE

# Preconditioned water-fat total field inversion: Application to spine quantitative susceptibility mapping

**Christof Boehm[1]** | **Nico Sollmann[2,3,4]** | **Jakob Meineke[5]** | **Stefan Ruschke[1]** |
**Michael Dieckmeyer[2]** | **Kilian Weiss[6]** | **Claus Zimmer[2,3]** | **Marcus R. Makowski[1]** |
**Thomas Baum[2]** | **Dimitrios C. Karampinos[1]**

[1]Department of Diagnostic and Interventional Radiology, School of Medicine, Klinikum rechts der Isar, Technical University of Munich, Munich, Germany

[2]Department of Diagnostic and Interventional Neuroradiology, School of Medicine, Klinikum rechts der Isar, Technical University of Munich, Munich, Germany

[3]TUM-Neuroimaging Center, Klinikum rechts der Isar, Technical University of Munich, Munich, Germany

[4]Department of Diagnostic and Interventional Radiology, University Hospital Ulm, Ulm, Germany

[5]Philips Research, Hamburg, Germany

[6]Philips Healthcare, Hamburg, Germany

**Correspondence**
Christof Boehm, Department of Diagnostic and Interventional Radiology, Klinikum rechts der Isar, Ismaninger Str 22, Munich 81675, Germany.
Email: christof.boehm@tum.de

Twitter: @BoehmChristof

**Funding information**
Philips Healthcare; H2020 European Research Council, Grant/Award Number: 677661

**Purpose:** To (a) develop a preconditioned water-fat total field inversion (wfTFI) algorithm that directly estimates the susceptibility map from complex multi-echo gradient echo data for water-fat regions and to (b) evaluate the performance of the proposed wfTFI quantitative susceptibility mapping (QSM) method in comparison with a local field inversion (LFI) method and a linear total field inversion (TFI) method in the spine.

**Methods:** Numerical simulations and in vivo spine multi-echo gradient echo measurements were performed to compare wfTFI to an algorithm based on disjoint background field removal (BFR) and LFI and to a formerly proposed TFI algorithm. The data from 1 healthy volunteer and 10 patients with metastatic bone disease were included in the analysis. Clinical routine computed tomography (CT) images were used as a reference standard to distinguish osteoblastic from osteolytic changes. The ability of the QSM methods to distinguish osteoblastic from osteolytic changes was evaluated.

**Results:** The proposed wfTFI method was able to decrease the normalized root mean square error compared to the LFI and TFI methods in the simulation. The in vivo wfTFI susceptibility maps showed reduced BFR artifacts, noise amplification, and streaking artifacts compared to the LFI and TFI maps. wfTFI provided a significantly higher diagnostic confidence in differentiating osteolytic and osteoblastic lesions in the spine compared to the LFI method ($p = .012$).

**Conclusion:** The proposed wfTFI method can minimize BFR artifacts, noise amplification, and streaking artifacts in water-fat regions and can thus better differentiate

between osteoblastic and osteolytic changes in patients with metastatic disease compared to LFI and the original TFI method.

# 1 | INTRODUCTION

The spine is the most frequent skeletal site for bone metastases.[1,2] In clinical routine, bone metastases are categorized to be either predominantly osteoblastic or osteolytic. Osteoblastic changes are characterized by the formation of new bone structures that might be weak and deformed while osteolytic meastastases are associated with bone destruction. The detection of bone metastases and their categorization into osteoblastic/osteolytic can be clinically important for several reasons, including the assessment of therapy response,[3] fracture risk,[4] or to support the search for an unknown primary tumor.[1,5] Due to its excellent soft tissue contrast, MRI is routinely used for assessing metastatic spread in vertebral bone marrow.[6] However, the delineation of osteoblastic and osteolytic metastases based on standard T1- and T2-weighted images cannot be achieved reliably.[6,7] Therefore, computed tomography (CT) remains the clinical standard for the osteoblastic/osteolytic categorization of bone metastases.

Susceptibility-weighted imaging (SWI) has been proposed and successfully applied for the MR-based differentiation of osteolytic and osteoblastic bone metastases at the spine.[7] Specifically, spine SWI has used the magnetic susceptibility to visualize the more diamagnetic properties of osteoblastic lesions (with locally increased mineralization) than osteolytic lesions (with locally decreased mineralization).[7] However, SWI only allows the qualitative assessment of bone mineralization changes and is also affected by changes in water-fat composition. Quantitative susceptibility mapping (QSM)[8] has been proposed to overcome the qualitative limitation of SWI. QSM is an MR technique that directly estimates the magnetic susceptibility and has been extensively used in the study of cerebral brain physiology,[9] pathology,[10] and function.[11] QSM has recently also been combined with water-fat separation techniques and has been applied in body regions outside the brain, for example, for measuring liver iron overload,[12-14] prostatic calcifications,[15] cartilage degeneration,[16] and bone density.[17-20]

QSM inverts the measured main magnetic field inhomogeneities, called the "field map," to the magnetic susceptibility map. The field map is thought to originate from two main sources: (1) the local field map that originates from MR-visible susceptibility sources within the region-of-interest (ROI) and (2) background field map contributions originating from MR-visible susceptibility sources outside the ROI, the concave geometry of the anatomy, the large susceptibility difference at the borders between tissue and air, flow, or breathing. In most imaging situations, the background field dominates the local field map by one or two orders of magnitude. Consequently, the background field map contributions need to be accounted for in order to estimate the local susceptibility map. A plethora of methods have been proposed to remove the background field contributions in a separate preprocessing step[21-25] before the local field inversion (LFI) is performed. However, background field removal (BFR) methods often suffer from an improper separation of background and local fields introduced by the assumptions of the adopted method. The improper separation of background and local fields can be particularly problematic at tissue-air boundaries.[8,12,21] Single-step methods have been proposed to simultaneously perform the steps of BFR and LFI to overcome the limitations associated with performing separately the two steps.[26,27] Most of the single-step methods implicitly remove the background field by a Laplacian operation. However, Laplacian-based single-step methods have shown to yield significantly reduced contrast in the finally estimated susceptibility maps in the applications also including spine QSM.[28-30]

A linear TFI algorithm has been proposed to perform the background field removal and estimate local susceptibility sources.[28] The proposed TFI algorithm reportedly overcomes the limitations of disjoint BFR and LFI and is able to robustly remove background field contributions. In addition, the adoption of a nonlinear QSM model has been proven to reduce streaking artifacts, particularly in regions with strong susceptibility sources and low SNR.[31] Strong susceptibility differences in the ROI are particularly common in body regions at the border of soft tissue and air (9.44 ppm)[32] or between tissue and the cortical bone shell (−2 ppm).[33] However, neither the linear TFI method nor the nonlinear QSM model can totally eliminate streaking artifacts in the presence of strong susceptibility differences. Therefore, the use of an iterative re-weighting method (MERIT)[31] was proposed and applied in both methods to alleviate remaining artifacts. In methods that use the Gauss-Newton approach for the minimization of the cost function, MERIT re-weights the voxels in the data

consistency term according to their residual error at each Gauss-Newton step. Voxels with high model mismatch are weighted down to reduce the influence of outliers in otherwise normally distributed data. However, MERIT can be subject to heuristic optimization and it can deteriorate the depiction of strong susceptibility sources.[34]

A recently proposed TFI method that directly estimates the susceptibility map from complex multi-echo gradient echo data (mcTFI)[34] combines the advantages of a nonlinear QSM model and a total field inversion method by reducing noise amplification and BFR artifacts. Additionally, mcTFI is able to reduce streaking artifacts without the use of the MERIT method. However, the original mcTFI can only be applied to regions with one chemical species and cannot account for the chemical shift of fat. Therefore, a new method is required to estimate the susceptibility map from complex multi-echo gradient echo data outside of the brain where both water and fat species are present.

Therefore, the purpose of this study is to (a) develop a water-fat total field inversion (wfTFI) method that directly estimates the susceptibility map from complex multi-echo gradient echo data in water-fat regions, and (b) to demonstrate the advantages of the developed method when applied in spine QSM of patients with metastatic bone disease where the the chemical shift of fat, large background fields, signal voids, and large susceptibility differences are present.
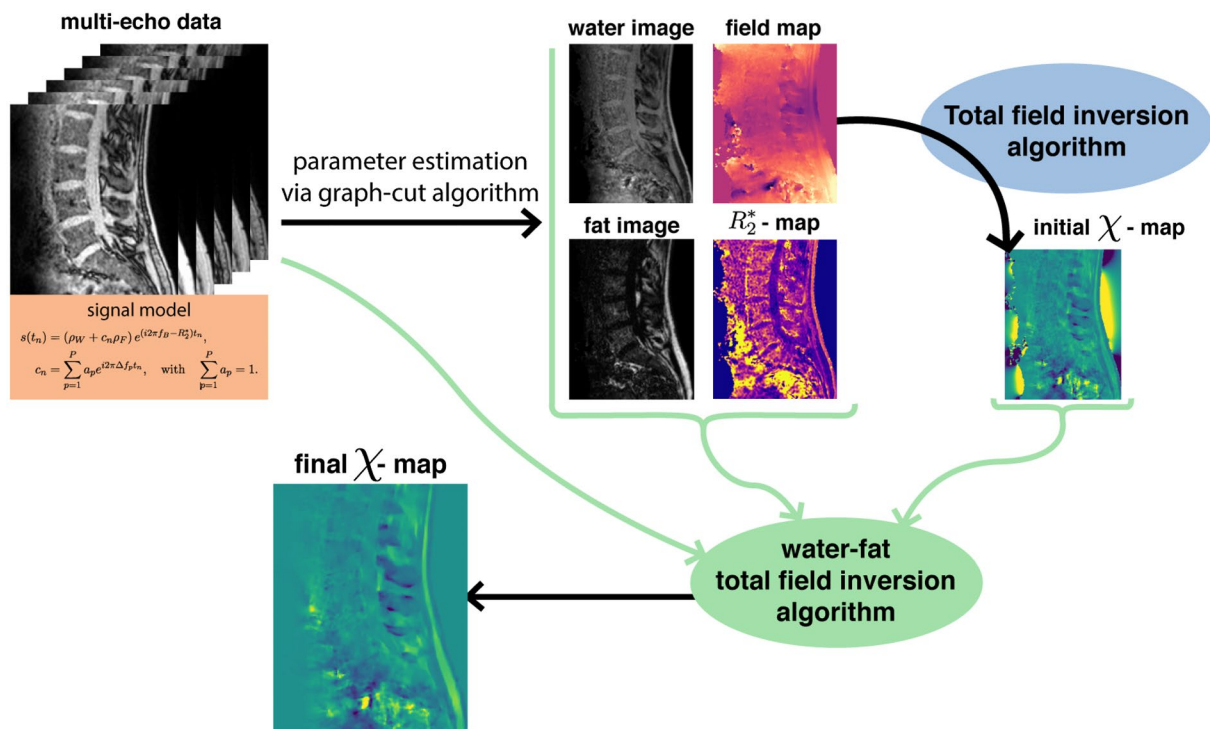
## 2 | METHODS

### 2.1 | Proposed preconditioned water-fat total field inversion algorithm

The proposed water-fat total field inversion (wfTFI) algorithm consists of 3 main steps (Figure 1). First, the water and fat image, field map, and $R_2^*$-map were estimated using a recently proposed graph-cut algorithm[35] and a water-fat signal model accounting for a single $R_2^*$ decay and employing a multi-peak fat model specific to bone marrow.[36] Second, an initial susceptibility map in the background and local region (see below regarding the determination of the background and local region) was estimated using a linear preconditioned TFI algorithm.[28] Finally, the susceptibility map was computed by estimating the susceptibility distribution directly from the complex multi-echo data by using a single-$R_2^*$ multi-fat-peak water-fat signal model minimizing the following preconditioned water-fat total field inversion cost function:

$$y = \arg\min_{y'} = \sum_{j=1}^{N_{echo}} || \left( \rho_W + c_n \rho_F \right) e^{-R_2^* t_j} e^{i t_j \; d * P y'} - S_j ||_2^2 + \lambda || M_g \nabla P y' ||_1 \tag{1}$$

$$c_n = \sum_{p=1}^{N_p} a_p e^{i 2\pi \Delta f_p t_j}, \quad \text{with} \quad \sum_{p=1}^{N_p} a_p = 1, \tag{2}$$



**FIGURE 1** Pipeline of the proposed water-fat TFI algorithm. The acquired multi-echo data are separated into water and fat image, field-, and $R_2^*$−map using a variable-layer single-min-cut graph-cut algorithm.[35] An initial $\chi$-map is estimated based on the field-map using the original TFI method.[28] Finally, the water-fat total field inversion algorithm is initiated with the initial $\chi$-map, water and fat image, and $R_2^*$-map. The final $\chi$-map is directly estimated from the multi-echo data

where $t_1, t_2, \ldots, t_N$ are the different echo times, $d$ is the dipole kernel, $P$ is the preconditioner, $M_G$ is the MEDI-like edge mask, [37] and $\nabla$ is the gradient operation,[8] $\rho_W$ and $\rho_F$ are the complex signal of the water and fat components assumed to have an equal transverse relaxation rate $R_2^*$. The fat spectrum was assumed to have $N_p$ spectral peaks with corresponding relative amplitudes $a_p$ and chemical shift $\Delta f_p$. The final QSM map was computed as $\chi = Py$.

By design, the preconditioner $P$ implicitly distinguishes between regions of background and local susceptibility sources.[28] To distinguish between background and local regions (region-of-interest (ROI)), a binary mask $M$ was calculated based on the maximum intensity projection (MIP) across echo times thresholded at 5% of its maximum value. Outside $M$, the preconditioner was calculated as a continuous cubic decay fitted to background susceptibility values obtained by the projection onto dipole fields method[22] as proposed in Ref. [38]. Inside $M$, the preconditioner was set to 1. Consequently, the preconditioner was automatically adapted to the ROI.

To obtain the edge mask $M_G$, the Sobel filter in all 3 spatial dimensions was applied on the MIP. The regularization parameter $\lambda$ was via L-curve analysis of a numerical simulation (see below) and was set to 100 for all data sets. The cost function in Equation (1) was minimized using the iterative Gauss-Newton algorithm with a conjugate gradient solver at each step. In total, 30 Gauss-Newton steps were performed.

## 2.2 | Comparison methods

The proposed wfTFI method was applied and compared to (1) a methodology combining the Laplacian boundary value (LBV)[21] method for BFR and MEDI for LFI (labeled as LBV+MEDI),[31] (2) a methodology combining the projection onto dipole fields (PDF)[22] for BFR and MEDI for LFI (labeled as PDF+MEDI), and (3) the original TFI methodology with MERIT (labeled as TFI).[28] All methods were initialized with a field map obtained by the aforementioned graph-cut method.[35]

The presently employed MEDI-regularized LFI used the following nonlinear formulation of the field to susceptibility inversion[31]:

$$\chi = \arg\min_{\chi'} = ||W(e^{id*\chi'} - e^{if_l})||_2^2 + \lambda||M_g\nabla\chi'||_1, \quad (3)$$

where $W$ is the magnitude weighting and $f_l$ is the local field map. The cost function was minimized with the aforementioned Gauss-Newton algorithm.

The original TFI algorithm was used as the third comparison method. The original TFI minimizes the following preconditioned linear formulation of the field to susceptibility inversion[28]:

$$y = \arg\min_{y'} = ||W(f_B - d*Py')||_2^2 + \lambda||M_g\nabla Py'||_1, \quad (4)$$

where the final QSM map was computed as $\chi = Py$. The same preconditioner $P$ was used as in the proposed wfTFI method. Due to the nonlinearity of the regularization term, the above cost-function was again minimized with the above Gauss-Newton algorithm. At each Gauss-Newton step, MERIT reweighting was applied to the magnitude weighting $W$, where each voxel was re-weighted according to their residual error.[31]

The regularization parameter $\lambda$ was determined via L-curve analysis of a numerical simulation (see below) and was set to 1/250 for MEDI and 1/2500 for TFI, respectively. The stopping criterion for both methods was a relative residual of $< 0.01$. The edge mask $M_G$ in the regularization term, represented by the second term in Equations (1), (3), and (4), was the same for all methods, including the proposed wfTFI. All processing was performed in Python 3.8 and CuPy 8.0.0[39] on a NVIDIA GeForce GTX 1080 Ti.

## 2.3 | Numerical simulation in the thoracolumbar spine

To investigate the difference between the presently proposed wfTFI method, the separate BFR and LFI methods and the formerly proposed TFI method, a numerical simulation based on the Duke phantom was performed using the annotated geometrical data from.[40] All of the body mesh data was converted into a three-dimensional volume corresponding to maps of 1.5 mm isotropic resolution. In order to assign bone marrow and the cortical bone shell with their respective susceptibility values, the binary erosion operation was applied on the bone mask and the difference between the original bone mask and the eroded mask was used as the mask for the cortical bone region. Each tissue was assigned with either their literature value or values extracted from in vivo scans as listed in Supporting Information Table S1. Based on the values in Supporting Information Table S1, fat fraction, $R_2^*$- and $\chi$-maps were generated. Additionally, SimpleITK[41] was used to manually add regions of air into the gastrointestinal system. To reduce the artificial piece-wise constant property of the generated maps, an independent Gaussian-filtered white noise distribution was added to each of the maps. The $\chi$-map was forward simulated to a field map $f_B$ using the dipole kernel in $k$-space. The widely used single-$R_2^*$ multi-fat-peak water-fat voxel signal model [42,43] was used to forward simulate the fat fraction $f_f$, $R_2^*$, and field maps to complex multi-echo data:

$$s(t_n) = \left((1-f_f) + c_n f_f\right) e^{\gamma t_n}, \quad \gamma = i2\pi f_B - R_2^*$$

$$c_n = \sum_{p=1}^{P} a_p e^{i2\pi\Delta f_p t_n}, \quad \text{with} \quad \sum_{p=1}^{P} a_p = 1. \quad (5)$$

The echo times were set to $TE_{min} = 1.1$ ms, $\Delta TE = 1.1$ ms. A field strength of 3 T and the aforementioned fat model specific to bone marrow were used. An additional parabolic signal drop in posterior-anterior direction was added to account for the signal drop observed in the in vivo spine scans due to the common lack of surface coils placed on top of patients (anterior body region). Independent Gaussian noise was added to the real and imaginary part of the echo data with an signal-to-noise ratio (SNR) of 50. The SNR was defined as the maximum signal amplitude of the first echo divided by the standard deviation. To obtain water- and fat-separated images, field map and $R_2^*$-map from the simulated multi-echo data, the aforementioned graph-cut based field-mapping method was used. Based on the maps estimated by the graph-cut method, the proposed wfTFI method was applied and compared to the aforementioned comparison methods (LBV+MEDI, PDF+MEDI, TFI). The estimated $\chi$-maps were visually examined for BFR and streaking artifacts and noise amplification.

## 2.4 | In vivo measurements

The aforementioned processing of graph-cut based field mapping and water-fat separation followed by LBV + MEDI, PDF + MEDI, TFI, and wfTFI QSM methods was applied to in vivo scans of a healthy volunteer and patients. Approval by the institutional review board (Klinikum rechts der Isar, Technical University of Munich, Munich, Germany) was granted for the patient scans and informed consent was received. The scanning was performed on a 3 T scanner (Ingenia, Philips Healthcare, Release 5.4, Best, The Netherlands) using a monopolar time-interleaved multi-echo gradient echo sequence,[44] acquiring 6 echoes in 2 interleaves with 3 echoes per interleave. For all subjects, the imaging parameters were set to $TE_{min} = 1.12$ ms, $\Delta TE = 0.96$ ms, orientation = sagittal, readout direction = anterior-posterior, $FOV = 219.6 \times 219.6 \times 79.2$ mm$^3$, and an isotropic acquisition voxel size of 1.8 mm.

In the patient study, only data were included from patients who received a CT and MRI examination, including $T_1$-weighted turbo spin echo (T1w TSE), $T_2$-weighted Dixon in-phase (T2w IP), and water (T2w water) from the standard clinical routine protocol. The CT scans were acquired within 30 days before or after the MRI due to clinically indicated reasons, including sagittal reformations of the spine (slice thickness of 3 mm). Specifically, 1 scan of the lumbar spine of a healthy volunteer and 10 scans of the spine of patients with osteolytic/osteoblastic changes due to metastatic disease were evaluated. The scans covered the lumbar spine in 7 patients, the cervical spine in 2 patients, the thoracic spine in one patient, and the lumbar spine in the volunteer.

The scans derived from the 10 scans in patients were evaluated and graded by two radiologists (a board-certified radiologist with 11 years of experience and a resident with 8 years of experience in neuroradiological imaging). The scans were read in a consensus-like setting and the readers were strictly blinded to the reports created during the clinical routine and to the characteristics of the metastases (osteolytic/osteoblastic) similiar to.[7] First, the CT images were evaluated via consensus reading in order to provide the reference standard for osteolytic and osteoblastic metastases. After an interval of about four weeks to avoid recall bias, the conventional MR sequences (T1w TSE, T2w IP, T2w water) and the QSM sequence results were separately evaluated for differentiating metastases between osteolytic and osteoblastic. In the reading of the conventional MR sequences, metastases that were predominantly hypointense on T1-weighted images and hyperintense on T2-weighted images were classified as osteolytic, and, conversely, metastases that were predominantly hypointense on T1- and T2-weighted images were classified as predominantly osteoblastic.[7] In the reading of the QSM maps, metastases were graded as osteoblastic if they were hypointense on MIP across echo times and hypointense on the QSM map, and, conversely, metastases that were hyperintense in the MIP and neutral on the QSM map (values around zero) were classified as osteolytic. The diagnostic confidence of the QSM methods to distinguish between osteolytic and osteoblastic changes was graded as 1 (low confidence), 2 (medium confidence), or 3 (high confidence). Additionally, the three $\chi$-maps estimated by the PDF+MEDI, TFI, and wfTFI QSM methods were graded for the overall image quality on a scale from 1 (low quality) to 3 (high quality). A Wilcoxon test was employed for comparing the diagnostic confidence and the image quality of the susceptibility maps derived with the wfTFI method and the PDF+MEDI method.

## 3 | RESULTS

### 3.1 | Numerical simulation in the thoracolumbar spine

Figure 2 compares the aforementioned QSM methods with respect to BFR artifacts, noise amplification, and susceptibility values. The first row of Figure 2 shows that the employed graph-cut based field mapping and water-fat separation method is able to yield a non-wrapped field- and fat fraction map. LBV+MEDI and PDF+MEDI show BFR artifacts in the whole ROI and significantly reduced susceptibility values of the vertebral bodies and the fat region surrounding the spinous processes. The TFI method does not suffer from BFR artifacts but shows noise amplification and further reduced susceptibility values in the spinous process fat region. The proposed wfTFI appears less noisy and shows reasonable susceptibility values in the vertebral bodies and spinous process fat region. Additionally, the wfTFI method shows
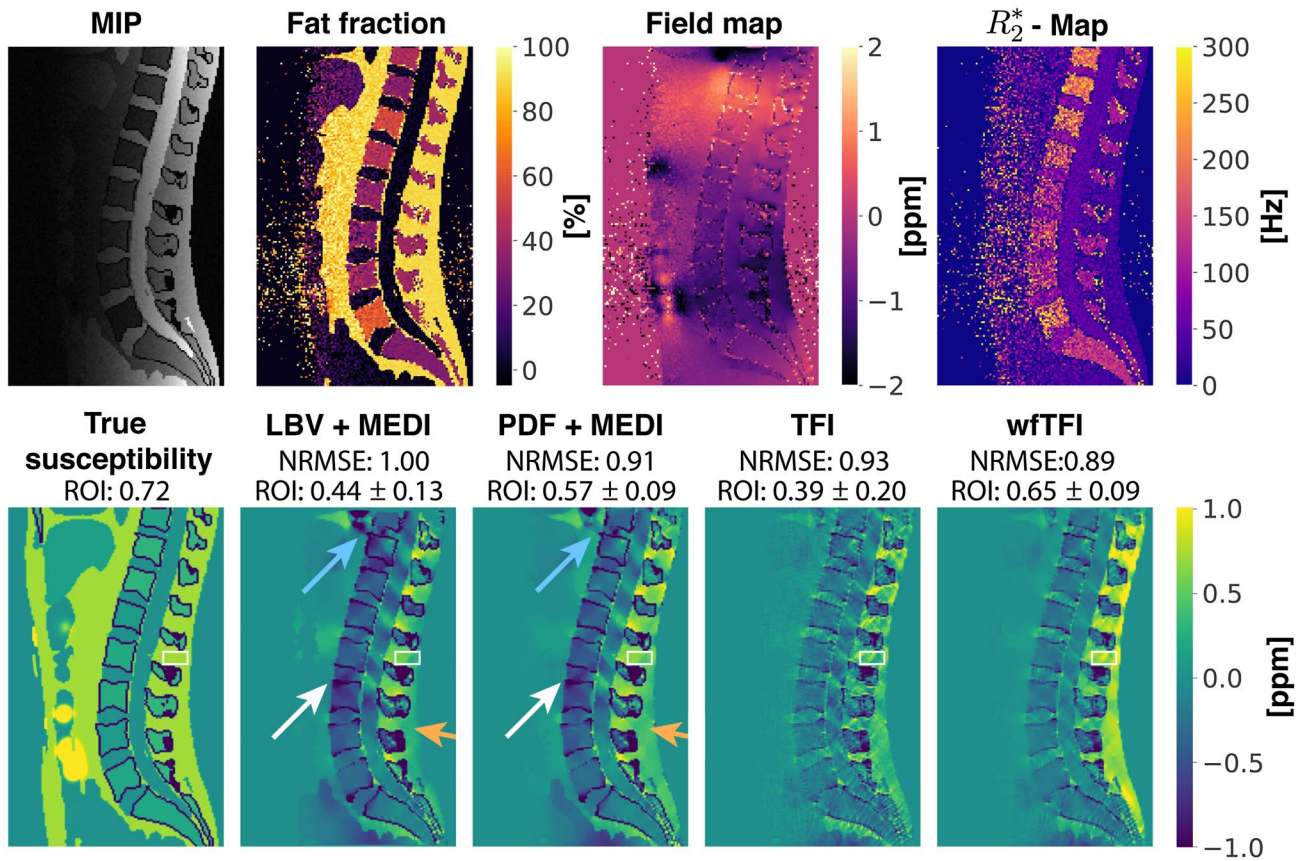
**FIGURE 2** Results of water-fat imaging (first row) and QSM (second row) results in the numerical multi-echo lumbar spine simulation. The first row shows the maximum intensity projection over echo times (MIP) of the 6 simulated echos and reveals the simulated cubic signal drop in posterior-anterior direction. Furthermore, the estimated fat fraction, field map, and $R_2^*$-map are shown in the first row. The graph-cut based field mapping is able to estimate a non-wrapped field map and fat fraction. In the LBV + MEDI and the PDF + MEDI method, BFR artifacts appear in the whole ROI. Both methods indicate an artifactual diamagnetic source present at the air-tissue interface to the lungs (blue arrow). Decreased susceptibility values can be observed in the center of the spine (white arrow) and inside all vertebral bodies. The simulated susceptibility of fat around the spinous processes (orange arrow) is significantly reduced in comparison to the true susceptibility. The TFI method does not show BFR artifacts but shows strongly elevated noise and reduced susceptibility values in the spinous process region. The wfTFI does not show BFR artifacts, yields reasonable susceptibility values inside the vertebral bodies and shows significantly reduced streaking, especially in cerebrospinal fluid. Furthermore, the susceptibility of fat surrounding the spinous processes is closer to the reference values when estimated by the wfTFI method in comparison to the other methods (susceptibility ROI values within the white box reported within the Figure)

significantly decreased streaking artifacts in comparison to all other methods, which can be best illustrated within in the cerebrospinal fluid region. A normalized root mean square error analysis (NRMSE) of the QSM maps yields an error of 0.89 for the proposed wfTFI method, 0.93 for TFI, 0.91 for PDF+MEDI, and 1.00 for LBV+MEDI.

## 3.2 | In vivo measurements

Figure 3 compares the QSM methods with respect to BFR artifacts, noise amplification, and streaking artifacts in a healthy volunteer. The first row shows that the employed graph-cut based field-mapping method is able to estimate water-fat-swap-free field-, fat fraction-, and $R_2^*$-map in an in vivo scan. The different QSM methods show the same

behavior as in the numerical simulation shown in Figure 2. LBV+MEDI and PDF+MEDI show severe BFR artifacts. Furthermore, they show strong streaking artifacts around air inclusions in the bowel at the bottom of the FOV. The TFI method significantly reduces the BFR artifacts while elevating the noise level. However, the TFI method still shows significant streaking around the air inclusion in the bowel. The proposed wfTFI method shows no noise amplification and the weakest streaking artifact from the air inclusion in the bowel, compared to the other methods.

Among the 10 patients (4 females and 6 males, mean age: $71.5 \pm 10.9$ years, age range: 49.2-83.3 years), 3 patients suffered from metastasized prostate cancer, 2 patients each from breast cancer and lung cancer. The other patients suffered from mouth floor carcinoma, kidney cancer, and a neuroendocrine tumor, respectively. Figure 4 compares the QSM
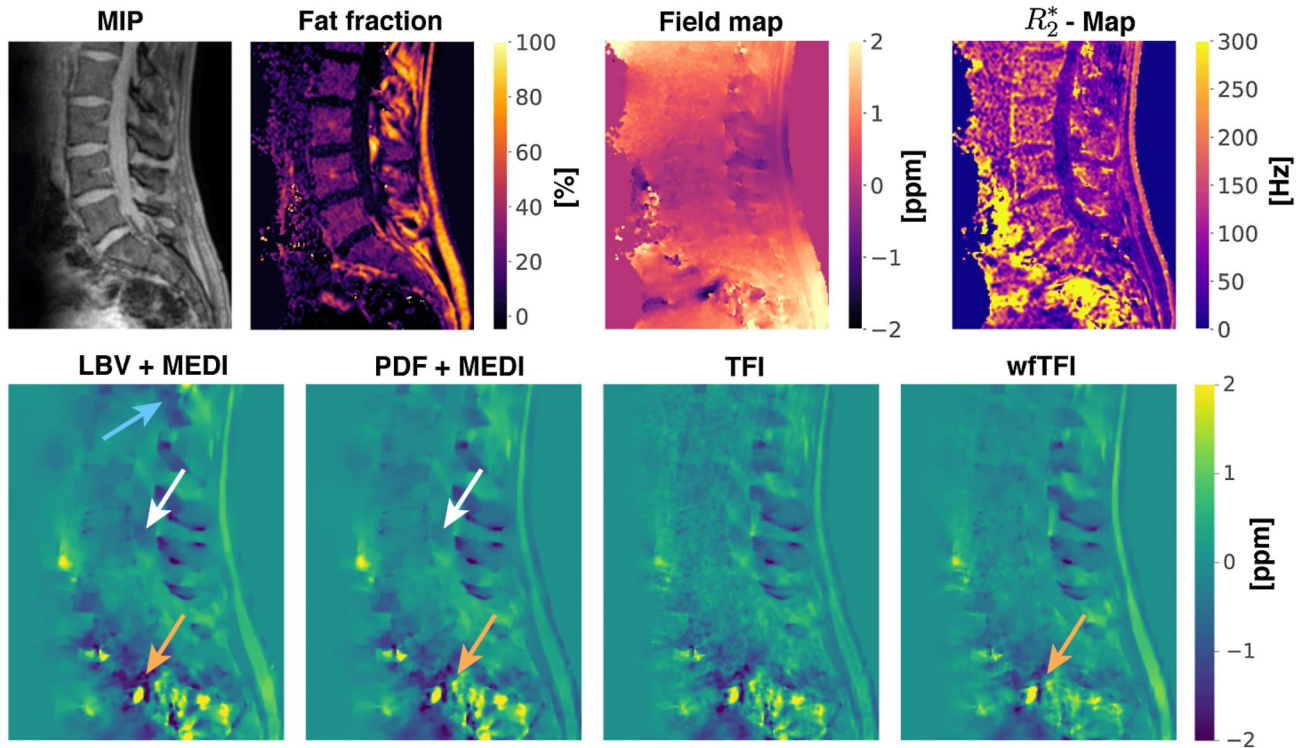
**FIGURE 3** Results of water-fat imaging (first row) and QSM (second row) in a healthy volunteer. The first row shows that the graph-cut based field mapping method is able to estimate a non-wrapped field map and fat fraction. In both QSM methods where BFR and LFI are independent steps, BFR artifacts appear in the whole ROI. In the LBV + MEDI method, there is an artifactual strong paramagnetic susceptibility source present in the spinous process region (blue arrow). In both BFR + LFI methods, a systematic underestimation of susceptibility values in the cerebrospinal fluid can be observed (white arrow). Air in the bowel causes strong streaking artifacts in the surrounding tissue (orange arrow). The streaking artifacts of the air in bowel are reduced when the original TFI method is used but the artifacts are still present. BFR artifacts are greatly reduced in the TFI method. However, the noise in the vertebral body region is elevated. The wfTFI method does not show BFR artifacts, shows no noise amplifications in the vertebral bodies, and shows the weakest streaking artifacts around the air inclusion in the bowel

methods in a subject with metastatic disease and mainly osteoblastic changes of the spine. The MIP shows that the vertebral bodies have almost no signal. Despite the low signal in the vertebral bodies, all QSM methods are able to pick up the strong diamagnetic property of the calcified vertebral bodies. However, the LBV + MEDI method shows a strong artifactual paramagnetic susceptibility source in the spinous process region of the T10 vertebra and the fat region at the L5 level (arrows). The PDF + MEDI shows a BFR artifact in the subcutaneous fat region of the T11 vertebra and the same BFR artifact as the LBV + MEDI method posterior to the L5 vertebra (white arrows). The TFI method yields a map without BFR artifacts. However, the noise in the TFI method is significantly elevated and it shows an artifactual increase of susceptibility values in the intervertebral discs (IVD). The proposed wfTFI method shows no BFR artifacts, minimal noise amplification, and reduced artifactual paramagnetic elevation in the IVDs.

Figure 5 plots the TFI susceptibility maps at different regularization parameters. When the regularization parameter $\lambda$ is increased in the TFI method in order to decrease the noise, the overall susceptibility contrast quickly

degrades (Figure 5). Furthermore, increasing the regularization parameter induces paramagnetic susceptibility values in the IVDs.
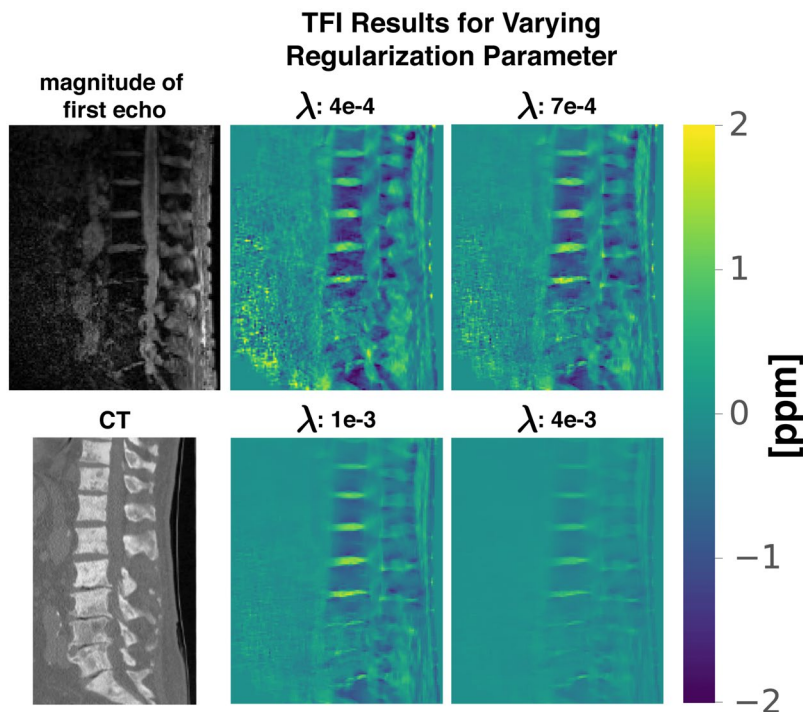
Figure 6 shows the water-fat imaging, clinical T1w TSE, T2w IP, T2w water, CT, and wfTFI results in a female patient diagnosed with breast cancer and both osteoblastic and osteolytic bone metastases at the lumbar spine. The osteoblastic components in the vertebrae L3-L5 according to CT show T1- and T2-hypointense correlates. The osteoblastic components are in good agreement with the results of the wfTFI QSM methods. The wfTFI QSM method is able to pick up intravertebral variations as present in the L2 vertebra, where a localized increased bone deposition can be observed in the posterior inferior part of the vertebra. This directly translates to diamagnetic values in the same region in the susceptibility of the wfTFI method.

Figure 7 shows the water-fat imaging, clinical T1w TSE, T2w IP, T2w water, CT, and wfTFI results in a female patient diagnosed with renal cancer and mainly osteolytic bone metastases of the T4 and T5 vertebral body. However, the clinical sequences suggest an osteoblastic lesion, since the lesion appears as T1- and T2-hypointense. The MIP together with
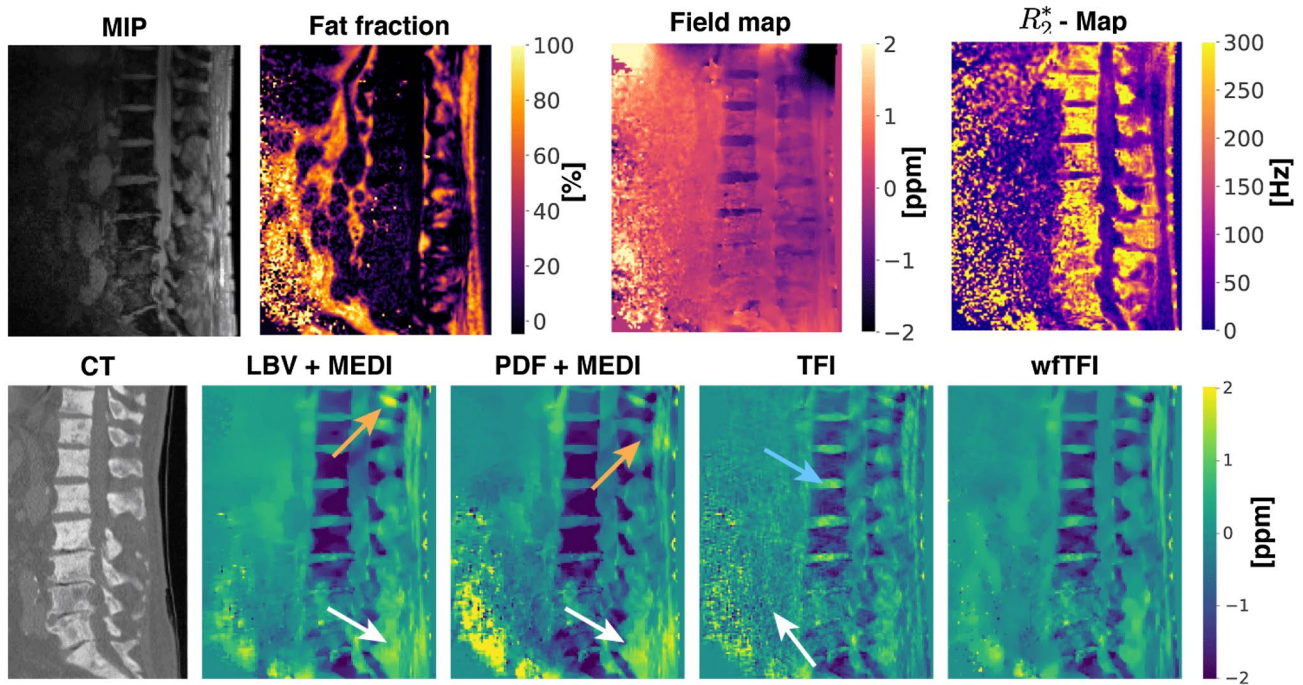
**FIGURE 4** Results of water-fat imaging (first row), CT (bottom left image), and QSM (second row) in a subject with mainly osteoblastic bone metastases. The fat fraction and $R_2^*$-map indicate a pathological change of the vertebral bodies by showing significantly reduced fat fraction and elevated $R_2^*$ values, respectively. In the estimation of the vertebral body susceptibility, all 4 QSM methods agree very well with the CT scan. However, the BFR + LFI methods show severe BFR artifacts, especially in the spinous process region of the T10 and T11 vertebra (orange arrows) in the LBV and PDF based maps, respectively, and the fat region in the height of the L5 vertebra (white arrow). The TFI method shows significant noise amplification in the anterior to the spinal cord (white arrow) and artifactual strong paramagnetic susceptibility values in all IVDs (blue arrow). The wfTFI shows no noise amplification, no BFR artifacts, and reduced artifactual paramagnetic elevation in the IVDs



**FIGURE 5** TFI results for varying the regularization parameter $\lambda$. When increasing the regularization parameter, the overall susceptibility contrast decreases while the noise artifacts are only slightly reduced. The artifactual paramagnetic estimation of the IVD regions remain strong for high regularization parameters

wfTFI suggests an osteolytic lesion, thus being in agreement with CT. Figure 8 shows the water-fat imaging, clinical T1w TSE, T2 IP, T2 water, CT, and wfTFI results in a male patient

diagnosed with prostate cancer and mainly osteoblastic bone metastases. The QSM map estimated by the proposed wfTFI method is in good agreement with the CT scan. It reveals
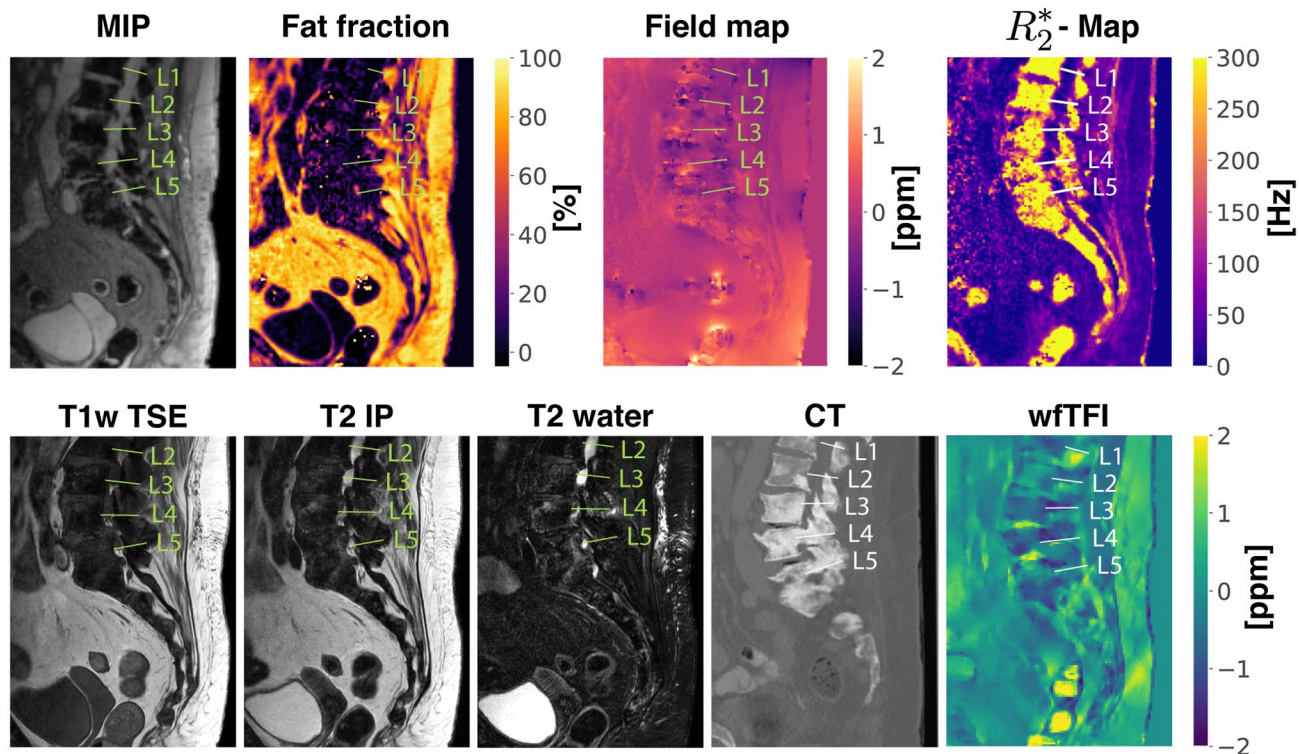
**FIGURE 6**   Results of water-fat imaging (first row), clinical T1w TSE, T2 IP, T2 water, CT, and QSM (second row) in a female patient diagnosed with breast cancer and mainly osteoblastic bone metastases along the displayed lumbar spine. In detail, the osteoblastic components in the vertebrae L3-L5 according to CT show T1- and T2-hypointense correlates, which are in good agreement with the results of the wfTFI QSM method that show diamagnetic values in the specific regions

the T12-L3 vertebra to be mainly osteoblastic and L4 and L5 to be mainly osteolytic. Additionally, the susceptibility map reveals the intradiscal air inclusions between sacrum-L5, L5-L4, L4-L3, and L3-L2, as verified by the CT scan. The detection of the air inclusion is not possible in conventional MRI sequences, MIP, or $R_2^*$-map.

The results of the reading of 10 subjects showed a mean diagnostic confidence of $2.1 \pm 0.7$ for PDF+MEDI, $2.6 \pm 0.66$ for TFI, and $2.8 \pm 0.4$ for wfTFI. The diagnostic confidence was significantly higher with the wfTFI method compared to the PDF+MEDI method ($p = .012$). The wfTFI method showed higher diagnostic confidence rating compared to the TFI method in 2 patient scans and equal diagnostic confidence to the TFI method in the rest. Furthermore, the image quality was estimated to be $1.1 \pm 0.3$ for PDF+MEDI, $2.4 \pm 0.66$ for TFI and $2.8 \pm 0.4$ for wfTFI. The image quality was also significantly higher with the wfTFI method compared to the PDF+MEDI method ($p < .001$). The wfTFI method increased the image quality rating compared to the TFI method in 3 patient scans and showed equivalent image quality to the TFI method in the rest. Within the reading of conventional sequences, only in 8/10 patients could the bone metastases correctly be identified as predominantly osteoblastic/osteolytic, while within the reading of the $\chi$-maps of the wfTFI method a correct classification in relation to CT was possible in all patients.

## 4 | DISCUSSION

The present study aimed to develop a method for improved QSM in water-fat regions. Specifically, the present study proposed to use a preconditioned water-fat TFI algorithm that directly estimates the susceptibility map from complex multi-echo gradient echo data. The study then examined the performance of the proposed wfTFI method in comparison to PDF + MEDI, LBV + MEDI, and a formerly proposed preconditioned linear TFI method in a numerical simulation, a healthy volunteer, and 10 patients with metastatic bone disease. The wfTFI results of the patients were graded by two senior radiologists with (a) respect to diagnostic confidence to distinguish osteolytic from osteoblastic bone metastases and (b) overall image quality. The proposed wfTFI method yielded a high diagnostic confidence and image quality for data derived from the patients, which may be due to the combination of advantages of formerly proposed methods, including the reduction of BFR artifacts, noise amplification, and streaking artifacts.

First, QSM based on the LBV and PDF both show BFR artifacts at the air-tissue interface of the lungs, the fat, and areas of hypointense values at some distance to convex geometry. In general, BFR artifacts appear as a slowly varying susceptibility distribution or as streaking artifacts at the local/background region interface. In the present study, the
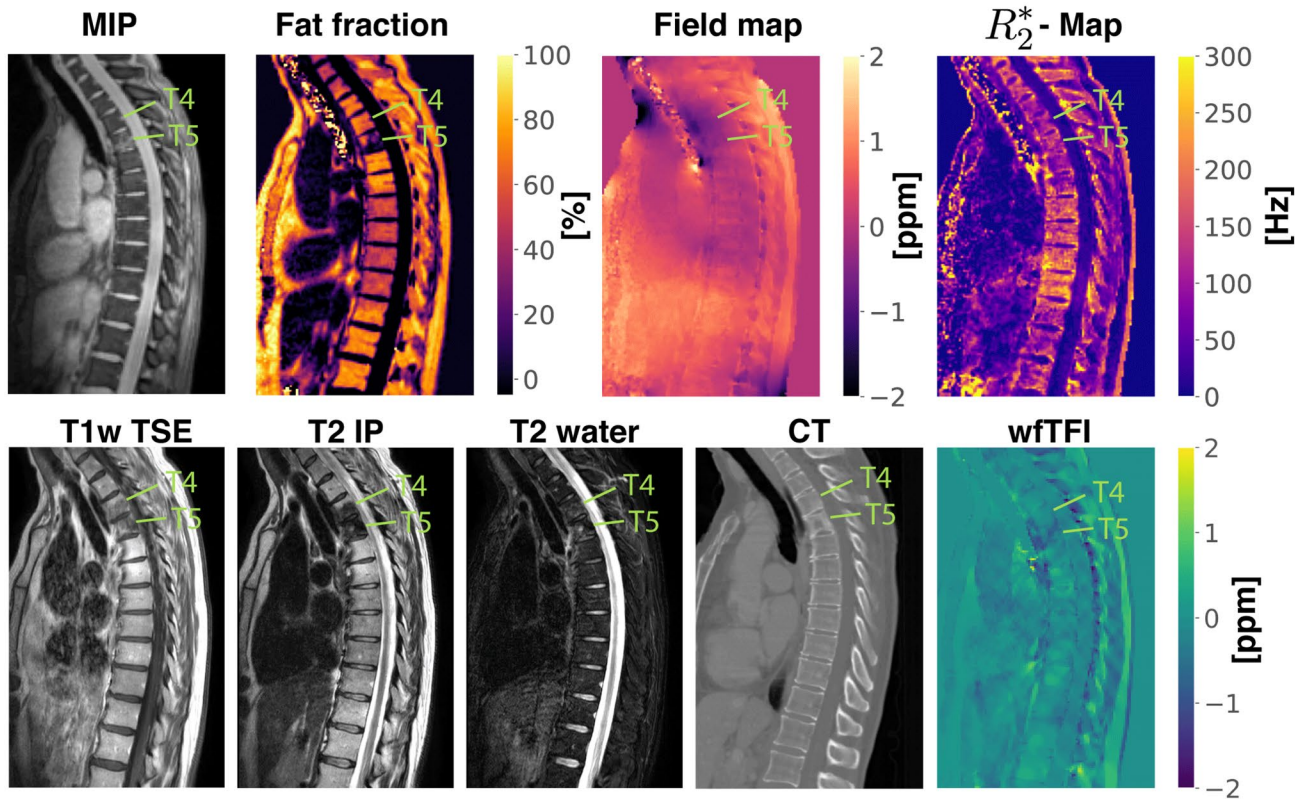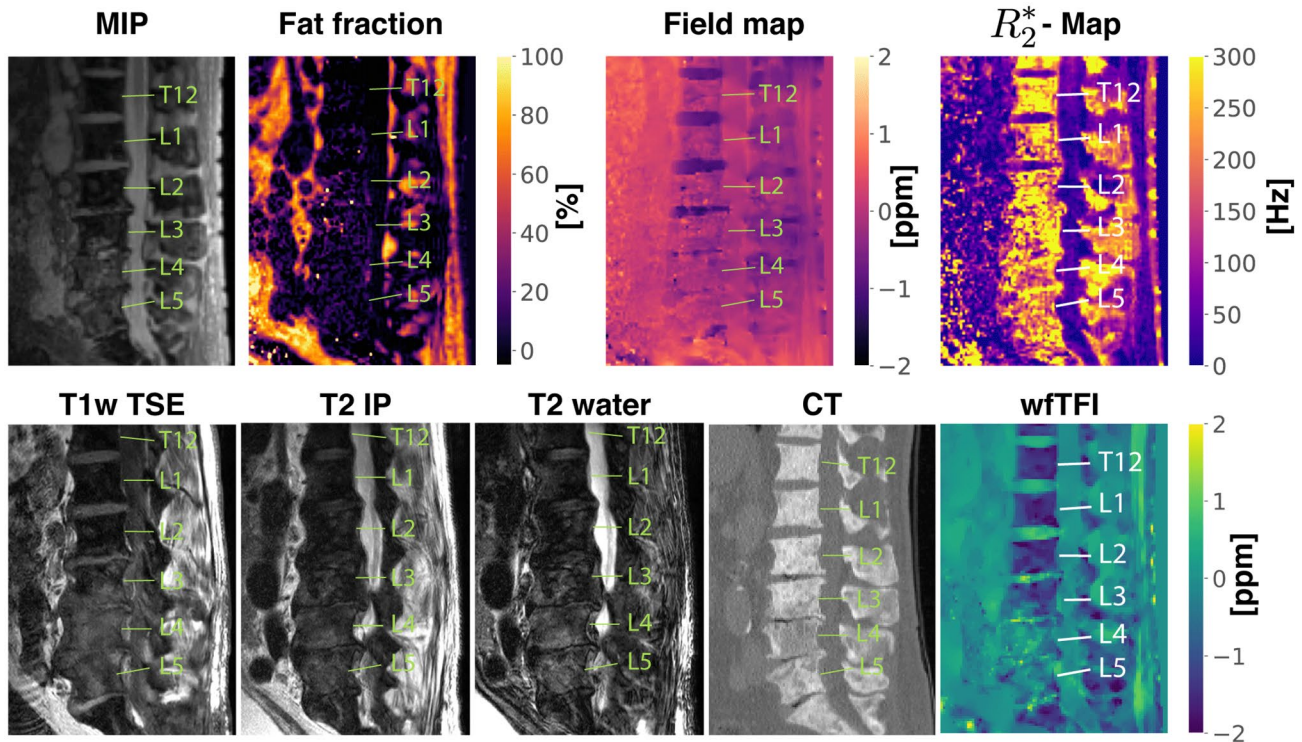
**FIGURE 7** Results of water-fat imaging (first row), clinical T1w TSE, T2w IP, T2w water, CT, and QSM (second row) in a female patient diagnosed with renal cancer and mainly osteolytic bone metastases of the vertebrae T4 and T5 according to CT. The metastatic lesion appears T1- and T2-hypointense, thus suggesting an osteoblastic mass. The results of the wfTFI QSM method and the MIP, however, suggest an osteolytic pattern, therefore being in agreement with CT as the reference standard

BFR artifacts in LBV+MEDI are more dominant than in PDF+MEDI. The BFR artifacts within LBV can be reduced by optimizing the local region mask at the cost of reduced visible tissue. However, it has been shown that the LBV method is problematic in body applications when the edges of the region mask contain strong susceptibility sources such as subcutaneous fat.[45] When the edges of the ROI mask contain strong susceptibility sources, the approximative assumption of the LBV method is violated: the local field in the selected boundary voxels is not much smaller than the local field. Hence, values close to the boundary are shifted towards zero. This limitation of the LBV can cause strong artifacts in body regions, when the ROI mask is not adjusted manually. A similar decrease in susceptibility values close to the ROI mask can be observed in the susceptibility map based on PDF BFR. However, in the PDF method, the underestimation of susceptibility in the ROI originates from the tendency of the PDF algorithm to overfit at the local/background region interface.[22,38] Consequently, susceptibility originating from the ROI is falsely estimated to originate from the background region. The significant reduction of BFR artifacts in the proposed wfTFI method originates from the simultaneous estimation of background and local susceptibility and was described in Ref. [28]. Furthermore,

in Ref. [28] the use of a preconditioner is proposed to increase the speed of convergence and is presently adapted in self-adapting variant similar to.[38] However, in the original TFI, the use of a preconditioner was mainly proposed to improve the rate of convergence and the use of the preconditioner was assumed to be optional. However, in the present study, the preconditioner has proven to be essential. When the preconditioner was removed, the estimation of local susceptibility was not possible and the result was dominated by artifacts. The preconditioner therefore contains the remaining necessary implicit assumption to distinguish regions of local and background susceptibility based on prior knowledge. However, the method was robust to the selection of the binary mask that distinguishes the above regions. The MIP across echo times thresholded at 5% of its maximum value has been proven to be robust across subjects and regions and was applied in all subjects and the simulation. In general, the results in the ROI have proven to be robust against the selection of the threshold. Furthermore, the BFR performance and susceptibility value estimation were robust against variations of the above binary mask selection.

Second, using a linear QSM model can (1) lead to the amplification of noise and (2) wraps in the field-map cannot be accounted for. While wraps in the field map can be

**FIGURE 8** Results of water-fat imaging (first row), clinical T1w TSE, T2w IP, T2w water, CT, and QSM (second row) results in a male patient diagnosed with prostate cancer and mainly osteoblastic bone metastases along the displayed thoracolumbar spine. The osteoblastic components in the vertebrae T12-L5 according to CT show T1- and T2-hypointense correlates that are in good agreement with the results of the wfTFI QSM method

eliminated by the correct parameter selection in the field mapping and water-fat separation method employed,[35] the noise amplification can be accounted for by an improved problem formulation. A nonlinear formulation of the field-to-source relation can be used to alleviate the abovementioned noise amplification problem.[31] The proposed wfTFI explicitly formulates the susceptibility estimation as a nonlinear problem by fitting the nonlinear water-fat signal model to the multi-echo gradient echo data. Additionally, the direct use of echo data benefits from the fact that the assumption of Gaussian noise is well justified in all voxels in contrast to the linear TFI model, where this assumption is only true in voxels with high SNR.[31] In body regions, voxels with low SNR frequently occur for different reasons, including (1) short $T_2$ tissues such as cortical bone in the ROI,[46] (2) air within in the ROI, for example, the lungs, air in the bowel or intraspinal air,[35] or (3) the general low signal strength due to coil sensitivity effects in standard clinical body MR protocols.[29] The estimation of susceptibility values within the original linear TFI method was not possible in regions with very low signal eg, anterior to the spine. QSM based on the linear TFI was not able to depict structures in this region while PDF+MEDI and the wfTFI method did. Furthermore, the linear TFI showed a significant overestimation in the IVDs in Figure 4. The proposed wfTFI showed that the formulation used in the present study can significantly reduce the noise

in QSM in regions with low SNR voxels that arise for the above reasons.

Third, the direct estimation of the susceptibility map from multi-echo has proven to reduce streaking artifacts originating from large susceptibility differences in the ROI. In QSM a plethora of methods have been proposed to reduce streaking artifacts originating from the zero-cone surface of the dipole kernel in *k*-space and many of them are based on regularization. One of the most well-established QSM regularization methods MEDI.[37] The assumption in MEDI regularization is that edges occurring in magnitude images are also likely to occur in the susceptibility map and was presently implemented in the wfTFI method. Despite the effectiveness of the MEDI regularization to reduce streaking artifacts, they still appear in many imaging situations. To further reduce streaking artifacts, the use of MERIT was proposed to alleviate remaining artifacts.[31] However, this method can lead to an artifactual distortion of regions with strong susceptibility sources[34] and the method itself requires appropriate optimization. A previous method ,called mcTFI, which directly estimates susceptibility from multi-echo data in the brain could reduce streaking artifacts, while the depiction of strong susceptibility sources was improved without the need for the MERIT method.[34] The proposed wfTFI shows the same reduction in streaking artifacts as shown in Figure 3 close to the air in the bowel and in all depicted spine regions in the

cerebrospinal fluid region. However, noteworthy is that the proposed wfTFI only optimizes over the susceptbility map after an initialization with the complex water and fat image and $R_2^*$-map, while mcTFI additionally optimizes over the complex signal and $R_2^*$.

Finally, the proposed wFTFI method shows improved diagnostic confidence in the particular application setting: the assessment of metastatic bone disease in order to distinguish between osteolytic and osteoblastic changes. It is clinically important to distinguish between osteolytic and osteoblastic metastases for several reasons: (1) vertebral bodies with osteolytic metastases have a higher probability of pathological fractures compared to osteoblastic metastases,[4] (2) osteolytic metastases can be subject to a sclerotic transformation after therapy,[3] and (3) the differentiation can support the search for an unknown primary tumor. The search for an unknown primary tumor is supported because osteolytic metastases are predominantly associated with renal, thyroid, colorectal, lung, and breast cancer in contrast to osteoblastic metastases that are predominantly associated with breast and prostate cancer.[1,5] The sensitivity to detect osteoblastic and osteolytic changes in standard T1- and T2-weighted spine MRI sequences has been estimated to be 89% and 73%, respectively.[7] In the present small patient study, the metastases in all patients could be correctly classified as predominantly osteolytic or osteoblastic based on the QSM maps of the proposed wfTFI method.

The present study has some limitations. First, in order to solve the proposed minimization problem in a reasonable timeframe a GPU with enough RAM is necessary. The depicted spine data sets needed approximately 6 GiB of RAM and the runtime for graph-cut based field-mapping and QSM was around 40 seconds on a NVIDIA GeForce GTX 1080 Ti consumer GPU used in the study. Second, the present wfTFI methodology would strongly benefit from a large-scale validation of its performance in more patients with bone metastases and other body QSM applications. Third, the improvement in the susceptibility value estimation was only evaluated in a qualitative setting. Therefore, the proposed method would benefit from a more quantitative validation. However, despite the fact that the proposed method is able to significantly reduce artifacts commonly present in the comparison methods and yields robust results across the present in vivo measurements, the aformentioned artifacts may still appear in some imaging situations.

In conclusion, the present study proposed a preconditioned water-fat total field inversion method for QSM in water-fat regions. The proposed method shows the following significant improvements over former proposed QSM methods: (1) it significantly reduces background field removal artifacts, (2) noise amplification, and (3) streaking artifacts, and thereby (4) improves the depiction of local susceptibility in water-fat regions.

# 5 | CONCLUSION

A preconditioned water-fat total field inversion method was proposed for QSM in water-fat regions. The proposed method shows the following significant improvements over former proposed QSM methods: (1) it significantly reduces background field removal artifacts, (2) noise amplification and (3) streaking artifacts while (4) improving the accuracy of the local susceptibility estimation

## CONFLICT OF INTEREST
Jakob Meineke is an employee of Philips Research and Kilian Weiss is an employee of Philips Healthcare. Dimitrios Karampinos receives grant support from Philips Healthcare.

## DATA AVAILABILITY STATEMENT
The Python implementation of all QSM methods as well as an example lumbar spine data set will be made freely available for download at https://github.com/BMRRgroup/wfTFI.

## ORCID
*Christof Boehm* http://orcid.org/0000-0003-1321-5804

## TWITTER
*Christof Boehm* @BoehmChristof

## REFERENCES
1. Yochum T, Rowe L. *Rowe's Essentials of Skeletal Radiology*. Philadelphia: Lippincott/Williams & Wilkins; 2005.
2. Kirchhoff SB, Becker C, Duerr HR, Reiser M, BaurMelnyk A. Detection of osseous metastases of the spine: comparison of high resolution multi-detector-CT with MRI. *Eur J Radiol*. 2009;69:567-573.
3. Kesavadas C, Santhosh K, Thomas B, et al. Signal changes in cortical laminar necrosis-evidence from susceptibility-weighted magnetic resonance imaging. *Neuroradiology*. 2009;51:293-298.
4. Freeman A, Sumathi V, Jeys L. Metastatic tumours of bone. *Surgery (Oxford)*. 2017;36.
5. Freyschmidt J. *Skeletterkrankungen: Klinisch-Radiologische Diagnose und Differenzialdiagnose*. Berlin, Germany: Springer; 2008.
6. Lange MB, Nielsen ML, Andersen JD, Lilholt HJ, Vyberg M, Petersen LJ. Diagnostic accuracy of imaging methods for the diagnosis of skeletal malignancies: a retrospective analysis against a pathology-proven reference. *Eur J Radiol*. 2016;85:61-67.

7. Böker SM, Adams LC, Bender YY, et al. Differentiation of predominantly osteoblastic and osteolytic spine metastases by using susceptibility-weighted MRI. *Radiology*. 2019;290:146-154.

8. Wang Y, Liu T. Quantitative susceptibility mapping (QSM): decoding MRI data for a tissue magnetic biomarker. *Magn Reson Med*. 2014;73:82-101.

9. Liu C, Li W, Tong KA, Yeom KW, Kuzminski S. Susceptibility-weighted imaging and quantitative susceptibility mapping in the brain. *J Magn Reson Imaging*. 2014;42:23-41.

10. EskreisWinkler S, Zhang Y, Zhang J, et al. The clinical utility of QSM: disease diagnosis, medical management, and surgical planning. *NMR Biomed*. 2016;30.e3668

11. Sun H, Seres P, Wilman A. Structural and functional quantitative susceptibility mapping from standard fMRI studies. *NMR Biomed*. 2016;30.e3619

12. Sharma SD, Hernando D, Horng DE, Reeder SB. Quantitative susceptibility mapping in the abdomen as an imaging biomarker of hepatic iron overload. *Magn Reson Med*. 2014;74:673-683.

13. Lin H, Wei H, He N, et al. Quantitative susceptibility mapping in combination with water-fat separation for simultaneous liver iron and fat fraction quantification. *Eur Radiol*. 2018;28:3494-3504.

14. Jafari R, Sheth S, Spincemaille P, et al. Rapid automated liver quantitative susceptibility mapping. *J Magn Reson Imaging*. 2019;50:725-732.

15. Straub S, Laun FB, Emmerich J, et al. Potential of quantitative susceptibility mapping for detection of prostatic calcifications. *J Magn Reson Imaging*. 2016;45:889-898.

16. Wei H, Lin H, Qin L, et al. Quantitative susceptibility mapping of articular cartilage in patients with osteoarthritis at 3T. *J Magn Reson Imaging*. 2018;49:1665-1675.

17. Dimov AV, Liu Z, Spincemaille P, Prince MR, Du J, Wang Y. Bone quantitative susceptibility mapping using a chemical species-specific $R_2^*$ signal model with ultrashort and conventional echo data. *Magn Reson Med*. 2017;79:121-128.

18. Diefenbach MN, Meineke J, Ruschke S, Baum T, Gersing A, Karampinos DC. On the sensitivity of quantitative susceptibility mapping for measuring trabecular bone density. *Magn Reson Med*. 2019;81:1739-1754.

19. Bray TJ, Karsa A, Bainbridge A, et al. Association of bone mineral density and fat fraction with magnetic susceptibility in inflamed trabecular bone. *Magn Reson Med*. 2019;81:3094-3107.

20. Jerban S, Lu X, Jang H, et al. Significant correlations between human cortical bone mineral density and quantitative susceptibility mapping (QSM) obtained with 3D cones ultrashort echo time magnetic resonance imaging (UTE-MRI). *Magn Reson Imaging*. 2019;62:104-110.

21. Zhou D, Liu T, Spincemaille P, Wang Y. Background field removal by solving the laplacian boundary value problem. *NMR Biomed*. 2014;27:312-319.

22. Liu T, Khalidov I, de Rochefort L, et al. A novel background field removal method for mri using projection onto dipole fields (PDF). *NMR Biomed*. 2011;24:1129-1136.

23. Özbay PS, Deistung A, Feng X, Nanz D, Reichenbach JR, Schweser F. A comprehensive numerical analysis of background phase correction with V-SHARP. *NMR Biomed*. 2016;30.e3550

24. Li W, Avram AV, Wu B, Xiao X, Liu C. Integrated laplacian-based phase unwrapping and background phase removal for quantitative susceptibility mapping. *NMR Biomed*. 2013;27:219-227.

25. Schweser F, Deistung A, Lehr BW, Reichenbach JR. Quantitative imaging of intrinsic magnetic tissue properties using MRI signal phase: an approach to in vivo brain iron metabolism? *NeuroImage*. 2011;54:2789-2807.

26. Langkammer C, Bredies K, Poser BA, et al. Fast quantitative susceptibility mapping using 3D EPI and total generalized variation. *NeuroImage*. 2015;111:622-630.

27. Chatnuntawech I, McDaniel P, Cauley SF, et al. Single-step quantitative susceptibility mapping with variational penalties. *NMR Biomed*. 2016;30:e3570.

28. Liu Z, Kee Y, Zhou D, Wang Y, Spincemaille P. Preconditioned total field inversion (TFI) method for quantitative susceptibility mapping. *Magn Reson Med*. 2016;78:303-315.

29. Diefenbach MN, Van A, Meineke J, et al. Vertebral column quantitative susceptibility mapping using joint background field removal and dipole inversion. *Proceedings 26*. Paris, France: Annual Meeting International Society for Magnetic Resonance in Medicine; 2018:0191.

30. Böhm C, Diefenbach MN, Meineke J, Haase A, Karampinos DC. Improved body quantitative susceptibility mapping by using a variable-layer single-min-cut graph-cut algorithm for field-mapping. *Proceedings 27*. Montreal, Canada: Annual Meeting International Society for Magnetic Resonance in Medicine; 2019:0693.

31. Liu T, Wisnieff C, Lou M, Chen W, Spincemaille P, Wang Y. Nonlinear formulation of the magnetic field to source relationship for robust quantitative susceptibility mapping. *Magn Reson Med*. 2012;69:467-476.

32. Collins CM, Yang B, Yang QX, Smith MB. Numerical calculations of the static magnetic field in three-dimensional multi-tissue models of the human head. *Magn Reson Imaging*. 2002;20:413-424.

33. Hopkins JA, Wehrli FW. Magnetic susceptibility measurement of insoluble solids by NMR: magnetic susceptibility of bone. *Magn Reson Med*. 1997;37:494-500.

34. Wen Y, Spincemaille P, Nguyen T, et al. Multiecho complex total field inversion method (mcTFI) for improved signal modeling in quantitative susceptibility mapping. *Magn Reson Med*. 2021;86:2165-2178.

35. Boehm C, Diefenbach MN, Makowski MR, Karampinos DC. improved body quantitative susceptibility mapping by using a variable-layer single-min-cut graph-cut for field-mapping. *Magn Reson Med*. 2021;85:1697-1712.

36. Ren J, Dimitrov I, Sherry AD, Malloy CR. Composition of adipose tissue and marrow fat in humans By1h Nmr At 7 Tesla. *J Lipid Res*. 2008;49:2055-2062.

37. Liu T, Liu J, de Rochefort L, et al. Morphology enabled dipole inversion (MEDI) from a single-angle acquisition: comparison with cosmos in human brain imaging. *Magn Reson Med*. 2011;66:777-783.

38. Liu Z, Wen Y, Spincemaille P, et al. Automated adaptive preconditioner for quantitative susceptibility mapping. *Magn Reson Med*. 2020;83:271-285.

39. Okuta R, Unno Y, Nishino D, Hido S, Loomis C. CuPy: a NumPy-compatible library for NVIDIA GPU calculations. In: Proceedings of Workshop on Machine Learning Systems (LearningSys) in The Thirty-first Annual Conference on Neural Information Processing Systems (NIPS). 2017.

40. Gosselin MC, Neufeld E, Moser H. Development of a new generation of high-resolution anatomical models for medical device evaluation: the virtual population 3.0. *Phys Med Biol*. 2014;59:5287-5303.

41. Yaniv Z, Lowekamp BC, Johnson HJ, Beare R. Simpleitk image-analysis notebooks: a collaborative environment for education and reproducible research. *J Digital Imaging*. 2017;31:290-303.

42. Yu H, Shimakawa A, McKenzie CA, Brodsky E, Brittain JH, Reeder SB. Multiecho water-fat separation and simultaneous $R_2^*$ estimation with multifrequency fat spectrum modeling. *Magn Reson Med*. 2008;60:1122-1134.

43. Bydder M, Yokoo T, Hamilton G, et al. Relaxation effects in the quantification of fat using gradient echo imaging. *Magn Reson Imaging*. 2008;26:347-359.

44. Ruschke S, Eggers H, Kooijman H, et al. Correction of phase errors in quantitative water-fat imaging using a monopolar time-interleaved multi-echo gradient echo sequence. *Magn Reson Med*. 2016;78:984-996.

45. Van AT, Diefenbach MN, Meineke J, Kooijman H, Haase A, Karampinos DC. Background field removal in the presence of subcutaneous fat in body QSM. In: 4th International Workshop on MRI Phase Contrast & QSM, Graz, Austria. 2016.

46. Fortier V, Levesque IR. Phase processing for quantitative susceptibility mapping of regions with large susceptibility and lack of signal. *Magn Reson Med*. 2018;79:3103-3113.

## SUPPORTING INFORMATION

Additional Supporting Information may be found online in the Supporting Information section.

**Table S1** Fat fraction, $R_2^*$ and χ values of different body structures used for the numerical simulation of multi-echo lumbar spine data. The values were taken from either the literature or extracted from in vivo scans of the specific anatomical structure